Programmable Protein-DNA Composite Nanostructures: from Nanostructure Construction to Protein-Induced Micro-Scale Material Self-Assembly and Functionalization

Weijun Zhou, Žiga Strmšek, Jaka Snoj, Miha Škarabot, and Roman Jerala*

The integration of DNA and protein-designed nanostructures represents a transformative approach to the development of programmable biopolymers for nanoscale construction. While DNA nanostructures excel in the readily programmable precision and scalability of base pairing, protein assemblies exploit the chemical diversity of amino acids for greater functional versatility. Here a platform is presented that unifies these two paradigms by combining coiled-coil protein origami with DNA nanostructures through orthogonal protein-protein (SpyCatcher-SpyTag) and protein-DNA (DCV-DNA) covalent conjugation strategies. This dual-functionalization strategy enables the construction of stable and versatile protein-DNA composites capable of hierarchical self-assembly. This shows that these composites drive the transformation of DNA nanotubes into large-scale, patterned nanofibers or nanorods, with the proteins regularly distributed over their surface and retaining their enzymatic and fluorescent functions. In addition, a DNA-luciferase circuit is developed through split enzyme reconstitution to achieve reversible regulation of enzymatic activity, highlighting the dynamic functionality of these composites. This introduces a modular approach to producing multifunctional bio-nanomaterials, highlighting the potential of protein-DNA composite nanostructures as a bridge between molecular design and functional nanomaterials and paves the way for the development of dynamic bio-devices and programmable biomaterials.

W. Zhou, Ž. Strmšek, J. Snoj, R. Jerala
Department of Synthetic Biology and Immunology
National Institute of Chemistry
Ljubljana SI-1001, Slovenia
E-mail: roman.jerala@ki.si
M. Škarabot
Condensed Matter Department
J. Stefan Institute
Jamova 39, Ljubljana SI-1000, Slovenia
R. Jerala
EN-FIST Centre of Excellence
Trg OF 13, Ljubljana SI-1000, Slovenia

1. Introduction

DNA nanotechnology leverages the natural base-pairing properties of DNA to construct precise and programmable nanoscale structures. A wide variety of two-dimensional- and -three-dimensional DNA-based nanostructures have been created, spanning from simple geometric shapes to complex functional devices.[1–6] Inspired by this, protein design based on complementary modules was introduced into nanotechnology and synthetic biology, using similar principles as in DNA nanostructures and focusing on the modular design of proteins that fold into predetermined shapes. This technique leverages the principles of natural protein folding and modular assembly with prospects for potential applications in biomedicine, biotechnology, and materials science.[7–9] One of the strategies in modular protein design that probably most strongly resembles DNA nanotechnology involves coiled-coil motifs—two or more α-helices winding around each other and forming a left-handed supercoil. These motifs can be engineered to interact selectively and predictably, much like complementary strands in DNA nanotechnology. Similar to DNA hybridization, coiled-coils also have specific pairing, which enables construction of designed proteins to self-assemble into precise geometries, such as tetrahedron,[10,11] bipyramid,[12] and triangle,[13] which opened the door for de novo protein design distinct from the design of globular protein folds developed using natural protein-based machine learning.[14]

Despite the common goal of achieving programmable nanoscale architectures, DNA and protein origami differ in their composition, fabrication methods, and practical applications. At its core, DNA nanotechnology utilizes base pairing as a driving force for precise self-assembly and usually requires slow annealing of the building block from high temperatures, which limits its functional diversity.[15,16] In contrast, protein assemblies offer an extensive toolkit of chemical functionalities, including enzymatic catalysis, binding specificity, and structural complexity. While peptide interactions are more complicated and less modular due to a larger diversity of amino acids and a larger number of conformers. However, even for proteins that have no similarity

to natural proteins, the design has been successfully addressed by machine-learning based strategies and modular topological designs.[17]

Combining DNA and polypeptide-based approaches opens up new possibilities for constructing hybrid nanostructures that leverage the advantages of both DNA and proteins.[18–22] For example, Niemeyer's group reported the purification of enzyme-functionalized DNA nanotechnology and observed an enhancement of enzyme activity.[23] DNA nanotechnology has been used to precisely regulate the distance and orientation between different enzymes, which provides a powerful tool for investigating the activity mechanisms of multi-enzyme systems.[24–27] Peptide-nucleic acid conjugates were also used to assemble large hybrid structures, aiming to use the programmability of DNA to direct peptide assembly.[28] However, most strategies use self-labeling protein tags (such as Snap-tag,[29] HaloTag,[30] streptavidin-binding peptide (SBP) tag,[31] etc.) or click chemistry[32] to connect protein to DNA, which requires costly DNA modification, and low conjugation yield.[33,34] In most studies, DNA provided a robust and programmable scaffold, while proteins offered a wide range of functionalities, including enzymatic activity, binding specificity, and structural diversity.[35–38] While few studies focused on co-interaction between proteins and DNA for forming large-scale composite structures.

Herein, we designed protein nanostructures capable of multiple covalent protein-DNA functionalization through an endonuclease single-stranded DNA (ssDNA) binding domain originating from Muscovy duck circovirus (DCV), covalent SpyCatcher-SpyTag conjugation systems, and fluorescent proteins (**Figure 1**). This platform enables efficient protein-ssDNA conjugation and robust protein-protein interactions, forming oligomers with diverse geometries (Schemes of examples shown in Figure 1D). Moreover, we demonstrated that the protein-DNA composites induced the self-assembly of DNA nanotubes into large-scale rigid nanorods or curly nanofibers, with uniform protein coverage and multilayer assembly. Bifluorescent protein labeling and enzyme immobilization at the surface of nanomaterials were validated through atomic force microscopy (AFM), total internal reflection fluorescence (TIRF) microscopy, and interference reflection microscopy (IRM) techniques. Functionalization with green fluorescent protein (GFP) and split nanoluciferase enabled enhanced bioluminescence resonance energy transfer (BRET) and reversible enzyme activity regulation. This work opens a new avenue for the oriented assembling of designed nanoscale devices and materials with potential applications in biomedicine, materials science, and synthetic biology.

2. Results

2.1. Protein-DNA Composites Design and Oligomer Assembly

DCV endonuclease domain recognizes sequence-specific ssDNA and reacts with the DNA backbone to form a covalent phosphotyrosine adduct (Figure 1A), providing a simple and efficient method for conjugating proteins with unmodified ssDNA.[39–41] Tetrahedral cage coiled-coil protein origami attracted attention due to its unique polypeptide chain topology and modular composition.[12,42] Each of its vertices can be addressed and modified individually in a defined geometry and stoichiometry. To
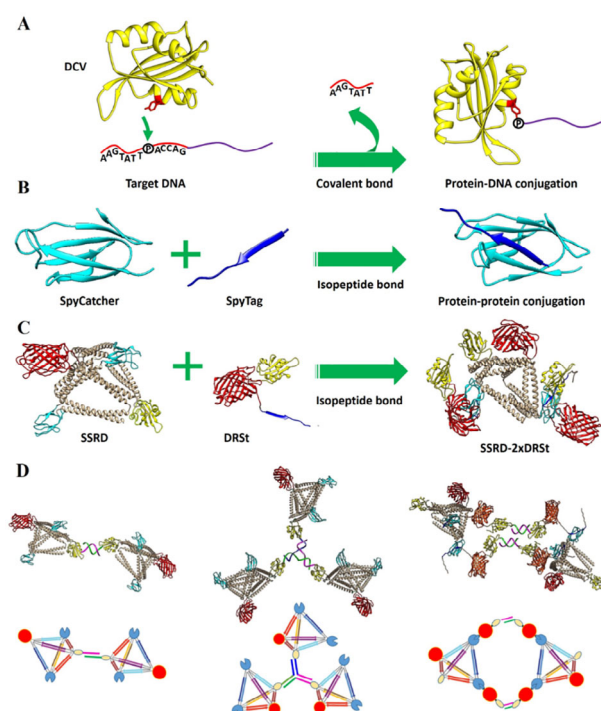

Figure 1. Molecular cartoon representation of protein-DNA building hybrid nanostructure self-assembly strategy. A) DNA-protein conjugation using DCV endonucleases domains. The reaction is initiated by the hydroxyl group of the tyrosine residue, which attacks the phosphorous atom in the DNA backbone and forms a covalent phosphotyrosine adduct. B) Protein-protein conjugates by SpyCatcher and SpyTag through isopeptide bond formation. C) Self-assembly of tetrahedral scaffold-positioned protein and DNA conjugation domains combining SSRD and DRSt through SpyCatcher-SpyTag action. D) Molecular models and schematic presentations of protein-DNA dimer and trimer assembling achieved via DNA hybridization. DCV, SpyCatcher, SpyTag, and RFP domains are colored in yellow, cyan, blue and red, respectively.

build a protein-DNA composite, where DNA oligonucleotides are introduced into the defined vertices of a protein tetrahedral scaffold, we first genetically fused the DCV domain at the C terminus of TET12SN(22CC), a stable tetrahedral protein (SASBDB accession code: SASDKR2).[42] DCV DNA conjugation reaction was completed within 2 h at 37 °C in the presence of Mn^{2+} ion. Size-exclusion chromatography coupled with multi-angle light scattering (SEC-MALS) and native polyacrylamide gel electrophoresis (SDS-PAGE) confirmed the DNA conjugation, as well as the ability of the protein-DNA composite to hybridize to the complementary DNA (Figure S1, Supporting Information). We also genetically inserted two, three, or four DCVs at different vertices of a tetrahedral cage at the position of linkers between the consecutive CC modules (22CC-2xDCV, 22CC-3xDCV, 22CC-4xDCV). Small-angle X-ray scattering (SAXS) confirmed that all the constructs folded into the desired shapes, where the inserted domains folded well and did not disrupt the self-assembly of the CC-based tetrahedral scaffold (Figures S1,S2, Supporting Information). For tetrahedra with multiple inserted DCVs, conjugation required overnight incubation to obtain high coupling efficiency (Figure S3, Supporting Information), probably due to the electrostatic repulsion and steric hindrance, as well as the

ADVANCED
SCIENCE NEWS
www.advancedsciencenews.com

NANO · MICRO
small
www.small-journal.com

reduced flexibility of DCV. After mixing two composites conjugated with complementary DNA_{S1} and DNA_{S2}, the main product was still a dimer; however, the proportion of oligomers gradually increased as the number of DCVs inserted into the tetrahedron increased from one to four, due to interactions between multiple protein hubs (Figure S4, Supporting Information). To assemble oligomers of larger dimensions, we designed double-stranded DNA (dsDNA) linkers with lengths of 15, 26, and 36 nm to connect protein-DNA composites (Figure S5, Supporting Information). High-molecular-weight polymers formed through this strategy, due to the flexibility of protein-DNA assemblies with different stoichiometry were obtained (Figure S6, Supporting Information). The same type of DNA conjugating domain introduced into a single protein only enables conjugation with the same type of DNA sequence, which may result in a heterogeneous assembly. Therefore, it would be beneficial to combine both DNA-protein as well as protein-protein conjugation strategies to obtain additional types of hybrid assemblies.

The SpyCatcher/SpyTag system is a robust protein conjugation tool that allows two protein domains to form a permanent covalent bond. SpyTag is a short peptide that can spontaneously form a covalent isopeptide bond with the SpyCatcher domain. (Figure 1B).[43,44] To accomplish more diversified self-assemblies and functionalization of hybrid nanostructures, we inserted one DCV, two SpyCatcher domains, and one red fluorescent protein (RFP) as functional domains at the four vertices of a tetrahedral cage to allow for multivalency, simultaneous conjugation with different DNA molecules and fluorescent monitoring. The de novo-designed protein was named SSRD (SpyCatcher-SpyCatcher-RFP-DCV, Supplementary Table S1, Supporting Information). SAXS analysis demonstrated that the SSRD folds with all four functional domains extended from the vertices of the tetrahedron (Figure S7,B, Supporting Information). SEC-MALS and native PAGE showed the successful conjugation of SSRD with the DNA to form $SSRD-DNA_{P1}$ and $SSRD-DNA_{P2}$ (Figure S7C,D, Supporting Information). Both composites were monodisperse, and the determined molecular mass matched the calculated size. After mixing, two protein-DNA composites formed a dimer by hybridizing complementary sequences in DNA_{P1} and DNA_{P2}. We also separately conjugated SSRD with DNA_{Y1}, DNA_{Y2}, and DNA_{Y3}, which enabled the construction of a Y-shaped protein-DNA trimer. AFM image confirmed the reproducible molecular shape of SSRD-DNA composites (**Figure 2A,B,C**; Figure S9, Supporting Information). Figure S10 (Supporting Information) showed that monomers are well-dispersed on the mica surface, while dimers and trimers appeared less homogeneous. This heterogeneity is likely results from the flexibility of the DNA overhangs and protein linkers, as well as structural rotation, overlap, and nonspecific adsorption during sample deposition. Confidently identified dimers and trimers were marked with white squares, and structures that we tentatively assigned as such—but with less certainty—were marked with red squares. ≈40% of the observed particles were identified as dimers and trimers (Table S7, Supporting Information). Although it is challenging to obtain fully uniform images for higher-order oligomers, the AFM data clearly showed clustered distributions and higher average heights that differs markedly from the monomeric form, supporting successful assembly (Figure S11, Supporting Information). The average lateral dimensions of

these composites range from 10 to 25 nm and agree with the dynamic light scattering measurements (DLS, Figure S12,S13,S14 and Table S8, Supporting Information) as well as dimensions obtained from the model. On the other hand, the average height of these composites is from 1.1 to 2.0 nm, which is lower than expected, likely due to the collapse of the tetrahedron during sample preparation. SSRD displayed a spherical structure, with RFP being more visible than a coiled-coil-based tetrahedron, due to its higher density. These results demonstrated that SSRD could bind diverse designed DNA sequences and had negligible effect on hybridization.

For orthogonal conjugation and more complex self-assemblies, we produced a construct DCV-RFP-SpyTag (DRSt). DRSt was rapidly conjugated to SSRD after mixing at a ratio of 2:1 through SpyCatcher-SpyTag reaction, and the size and shape of the product were confirmed by SAXS (Figure S8, Supporting Information). Different ssDNAs can be conjugated to either SSRD or DRSt, which introduces an additional assembly layer. After attaching DRSt, both protein-DNA dimer and trimer increased in size (Figure 2D,E,F). AFM images showed that with DNA conjugated to DRSt, $SSRD-2xDRSt-DNA_{P1}$ and $SSRD-2xDRSt-DNA_{P2}$ formed oligomers, based on the intermolecular hybridization (Figure 2G; Figure S9–S11, Supporting Information). Those results demonstrate that protein building blocks can be functionalized for protein-protein or protein-DNA conjugation at the vertices of tetrahedral cages through genetic encoding, DNA hybridization, or protein-protein conjugation enabling the construction of multi-layered self-assemblies forming diverse shapes.

2.2. Protein-DNA Composites Form Nanofiber and Nanorod Assemblies

While the protein-DNA composites exhibited well-defined topology and successful hybridization at the nanoscale, we next explored whether these modular constructs could serve as structural regulators to direct the organization of larger DNA-based architectures. However, the intrinsic flexibility of peptide linkers between functional domains limited the formation of well-defined, rigid oligomeric structures at greater scales. To overcome this, we employed a preassembled DNA nanotube scaffold, as developed by Green et al.[45,46] to provide a programmable and rigid framework. We hypothesized that by leveraging the orthogonal and multivalent binding capabilities of the protein-DNA composites—through both DNA hybridization and covalent protein interactions—we could guide the reorganization and morphological transformation of DNA nanostructures into higher-order materials. The building block of the DNA tube consists of five unique DNA strands with a length of 14.3 nm, and the programmed interactions between the sticky ends led to the assembly of a tubular structure. **Figure 3A** shows the design of a DNA scaffold, adapted from ref 45. DNA_{T1} was split into two strands (DNA_{T1a-P1} and DNA_{T1b}), with a standout overhang (P1) for protein attachment. IRM and AFM were used to characterize the morphology of DNA nanotubes (Figure 3B). In TAE-Mg buffer, DNA nanostructure formed nanotubes (up to 2 μm), slightly shorter than in the previous reports (average of 5 μm), likely due to the interference of standout overhangs. Interestingly, we
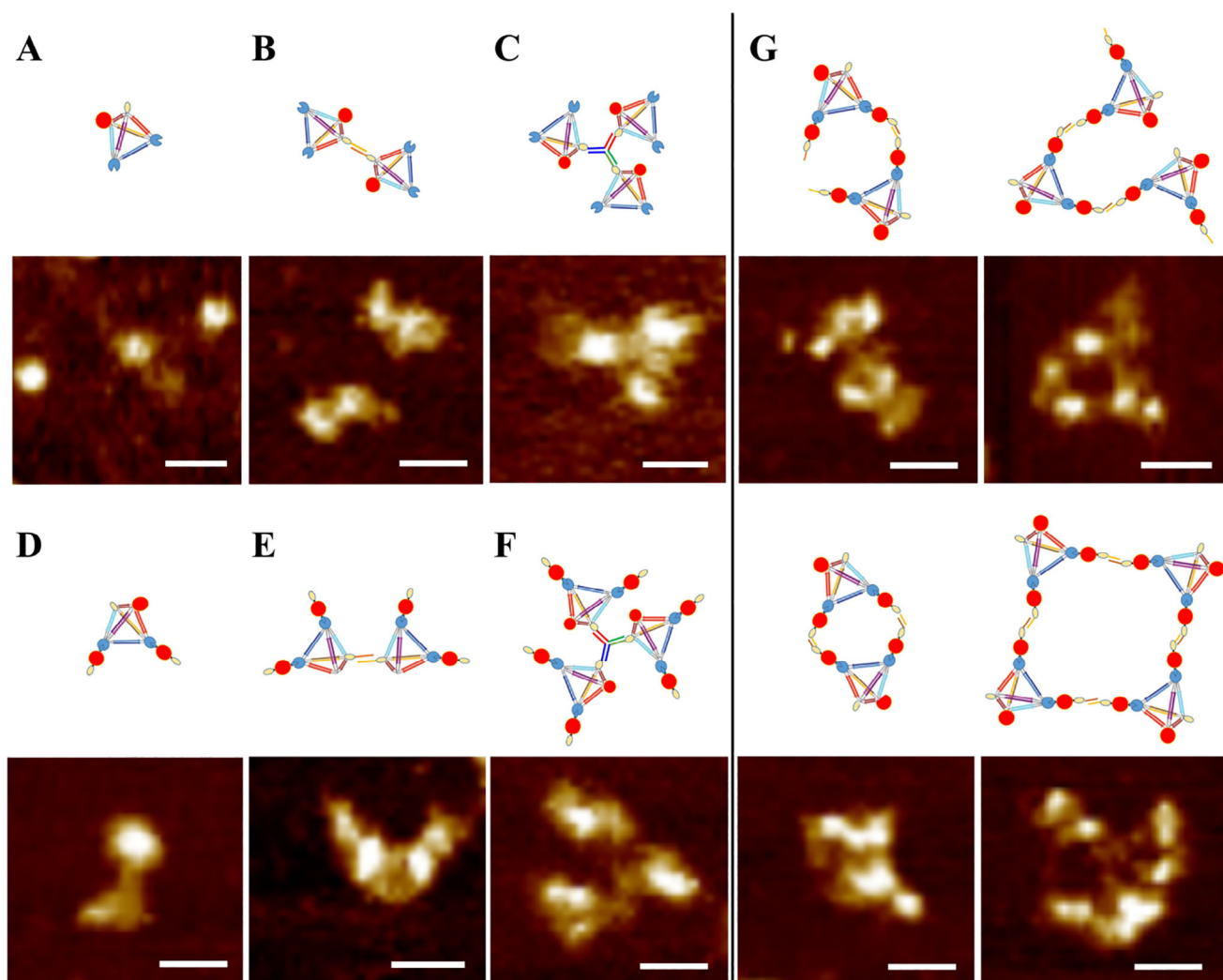
Figure 2. Molecular cartoon representations and AFM images of different protein-DNA composite oligomers: A) SSRD, B) SSRD-DNA dimer, C) SSRD-DNA trimer, D) SSRD-2xDRSt, E) SSRD-2xDRSt-DNA dimer (DNA conjugated to SSRD), F) SSRD-2xDRSt-DNA trimer (DNA conjugated to SSRD), G) Possible structural motifs of SSRD-2xDRSt-2xDNA oligomer (DNA conjugated to DRSt). Scale bar: 20 nm.

discovered that when annealed in a concentrated buffer (10xTAE-Mg), these small DNA tubes formed nanobelts with a widths range from 0.7 to 1.2 µm, heights of 2 nm, and lengths up to 50 µm (Figure 3C). The nanobelts could be observed under IRM, while the small nanotubes were barely visible. We propose that a 10-fold buffer concentration screened the electrostatic interactions between DNA nanotubes, leading to the reorganization of the assembly.

Furthermore, we attempted to attach SSRD-DNA$_{P2}$ to the surface of DNA nanostructures. Surprisingly, we discovered that protein-DNA composites induced the self-assembly of DNA nanostructure and significantly modified its morphology (Figure 3D). In TAE-Mg buffer, DNA nanotubes formed hair-shaped curvy fibers that extended up to 20 µm in length and 3.4 nm in height. After mixing, SSRD-DNA$_{P2}$ attached to the surface of the DNA tube via DNA hybridization, serving as the nucleation centers, which gradually grew into larger structures. Real-time TIRF microscopy recorded the formation process of

the nanofibers by detecting the fluorescence signal of RFP (Video 1, 2, and 3). Hair-shaped curvy fibers ripened with time and were homogeneously covered by protein-DNA composite after overnight incubation at 4 °C (Figure 3E). The fluorescence background was also reduced significantly since SSRD-DNA$_{P2}$ was concentrated at the surface of the fiber (Figure S15, Supporting Information). On the other hand, SSRD-DNA$_{P2}$ triggered the DNA nanobelts to reorient into rigid nanorods in 10xTAE-Mg buffer. TIRF and AFM images showed that protein-DNA nanorods had an average height of 4.8 nm, length of up to 50 µm and width of up to 0.7 µm (Figure 3F). Similar to the structure in TAE-Mg buffer, the surface of nanorods was uniformly covered by a fluorescent protein. Video 4 shows the reorientation of the nanorods. Although the changes in morphological structure were less obvious under TIRF, nanorods exhibited strong fluorescence after assembling with SSRD-DNA$_{P2}$. Similarly, DRSt-DNA$_{P2}$ also triggered the self-assembly of Protein-DNA nanofiber and nanorod in 1xTAE-Mg buffer and 10xTAE-Mg buffer,
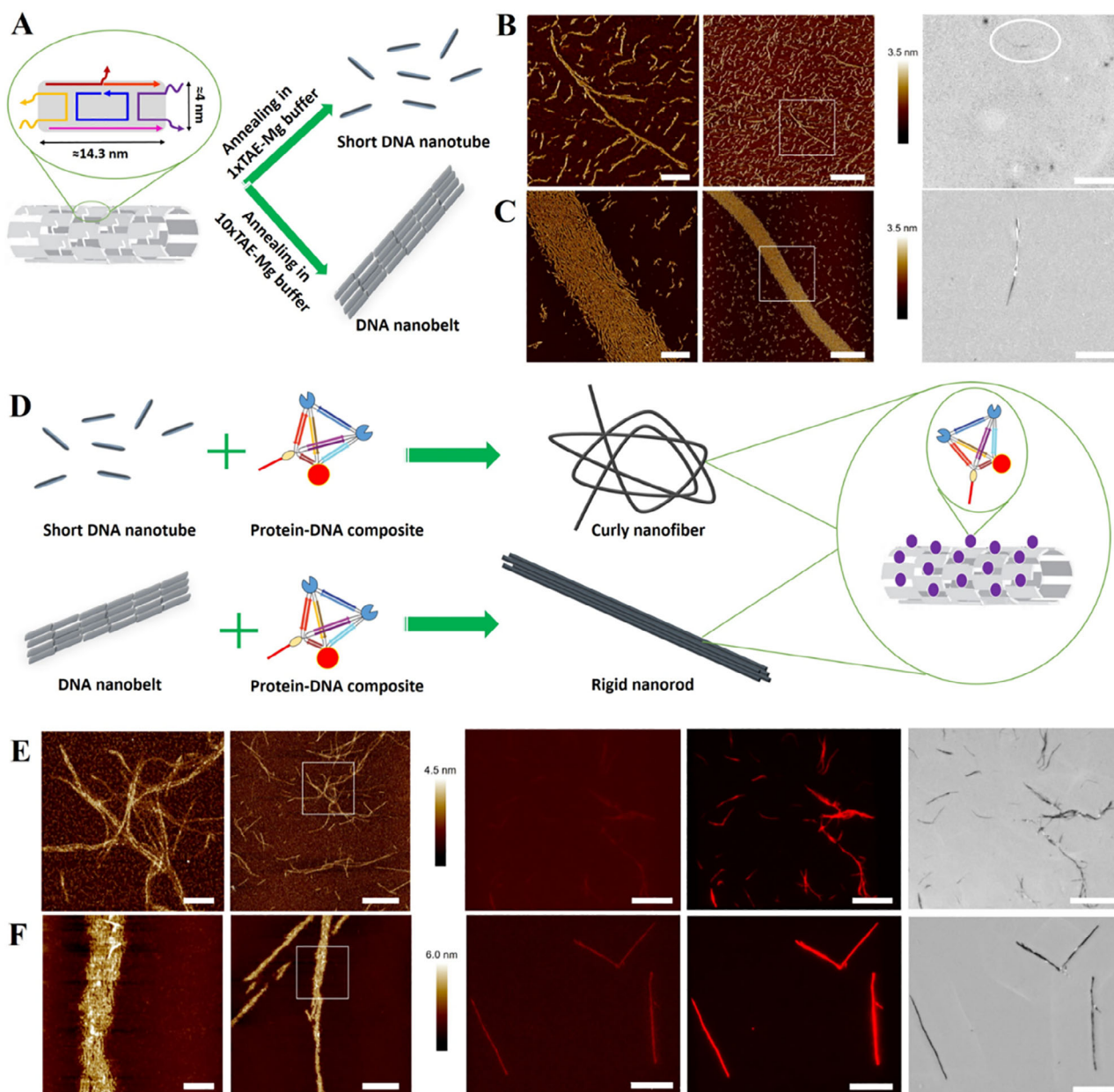
Figure 3. DNA nanostructure and protein-DNA composite self-assembly into different nanostructures. A) Via programmed interactions of sticky ends, the DNA building blocks form short nanotubes in 1xTAE-Mg buffer and nanobelt in 10xTAE-Mg buffer, separately. B) Morphology characterization of DNA nanotube in 1xTAE-Mg buffer. Left: AFM image at the scale of 3 × 3 µm, scale bar: 0.5 µm; middle: AFM image at the scale of 10 × 10 µm, scale bar: 2 µm, the 3 × 3 µm image scanning range was marked with a white square (average height: 1.5 nm, average width: 50 nm); right: IRM image, scale bar: 10 µm. DNA tube is barely visible and marked with a white circle. C) Morphology characterization of DNA nanobelt in 10xTAE-Mg buffer. Left: AFM image at the scale of 3 × 3 µm, scale bar: 0.5 µm; middle: AFM image at the scale of 10 × 10 µm, scale bar: 2 µm, the 3 × 3 µm image scanning range was marked with a white square (average height: 2 nm, width range: 0.7-1.2 µm); right: IRM image, scale bar: 10 µm. D) After mixing with protein-DNA composites, DNA nanotube or nanobelt further self-assemble into curly nanofiber or rigid nanorod, respectively. E,F) Morphology characterization of SSRD functionalized nanofiber (E) and nanorod (F). From left to right: AFM image at the scale of 3 × 3 µm, scale bar: 0.5 µm; AFM image at the scale of 10 × 10 µm, scale bar: 2 µm, the 3 × 3 µm image scanning range was marked with a white square; TIRF image excited by 488 nm laser; TIRF image excited by 561 nm laser; IRM image. Scale bars of TIRF and IRM are 10 µm.

separately (Figure S18A,B,C, Supporting Information). TIRF detected bright red fluorescence of RFP evenly distributed on the surface. Here, protein-DNA composites serve a dual role: they act as programmable connectors that drive assembly via DNA hybridization, and as functional modules that impart signaling capability.

Several TAE-Mg buffer concentrations were tested to better understand the mechanism underlying the structural
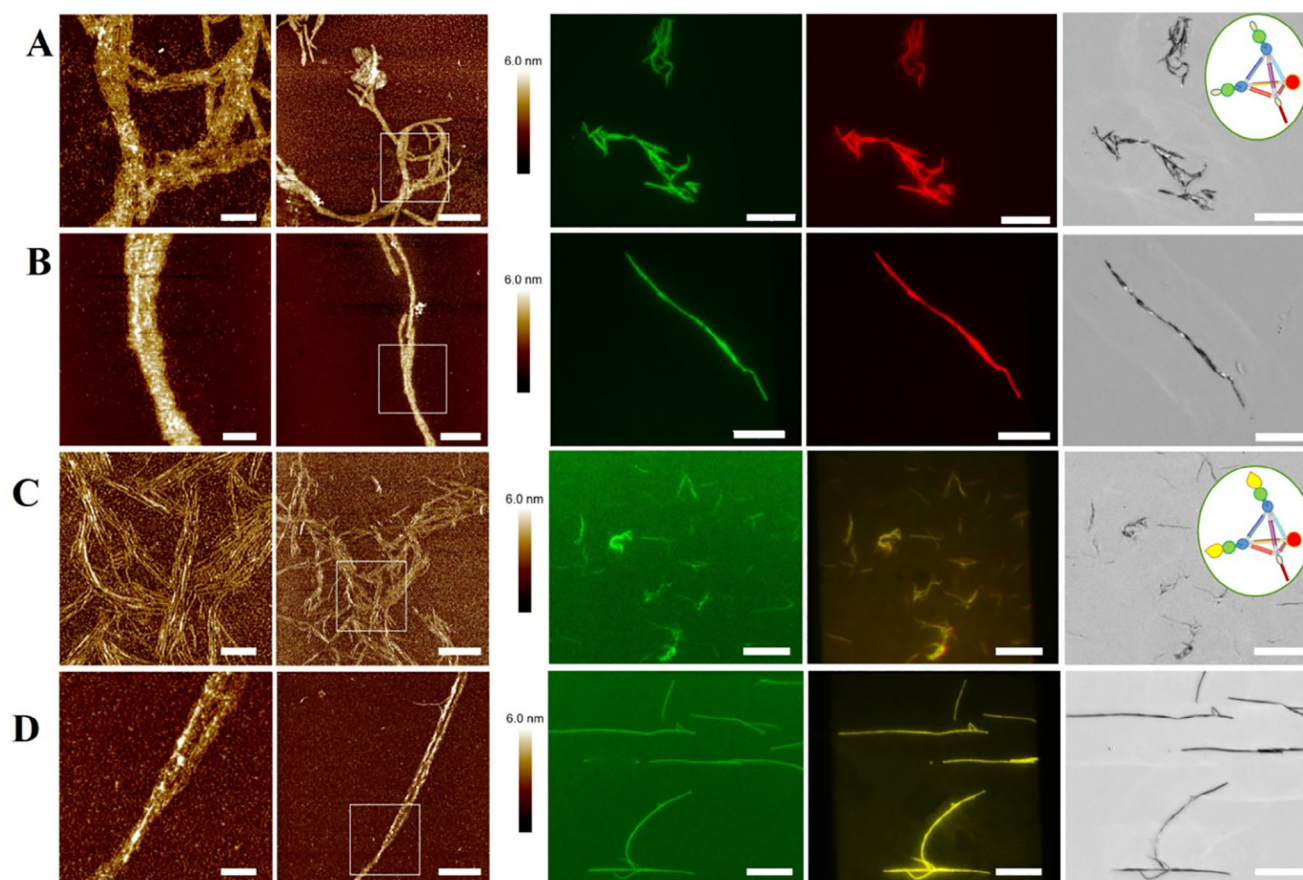
Figure 4. Morphology characterization of dual-fluorescent protein or enzyme functionalized nanofiber and nanorod. A,B) Morphology characterization of SSRD-2xDGSt functionalized nanofiber in 1xTAE-Mg buffer (A) and nanorod in 10xTAE-Mg buffer (B). From left to right: AFM image at the scale of 3 × 3 µm, scale bar: 0.5 µm; AFM image at the scale of 10 × 10 µm, scale bar: 2 µm, the 3 × 3 µm image scanning range was marked with a white square; TIRF image excited by 488 nm laser; TIRF image excited by 561 nm laser; IRM image. Scale bars of TIRF and IRM are 10 µm. The schematic shows the structure of SSRD-2xDGSt-DNA$_{P2}$. C,D) Morphology characterization of SSRD-2xLucGSt functionalized nanofiber (C) and nanorod (D). From left to right: AFM image at the scale of 3 × 3 µm, scale bar: 0.5 µm; AFM image at the scale of 10 × 10 µm, scale bar: 2 µm, the 3 × 3 µm image scanning range was marked with a white square; TIRF image without any laser (After mixing nanostructures with the Nano-Glo luciferase assay mixture, GFP was excited by the strong bioluminescence at 460 nm); Overlays of TIRF images excited by 488 and 561 nm laser; IRM image. Scale bars of TIRF and IRM are 10 µm. The schematic shows the structure of SSRD-2xLucGSt-DNA$_{P2}$.

transformation of DNA nanostructures. We found that in 2xTAE-Mg buffer, DNA nanostructures formed hair-shaped fibers even in the absence of protein-DNA composites, likely due to non-specific electrostatic interactions promoting lateral association. When SSRD-DNA$_{P2}$ was added in excess to these fibers, most—but not all—structures were coated with fluorescent protein. We hypothesize that the reduced exposure of ssDNA overhangs after fiber formation may have inhibited complete hybridization with the protein-DNA complex. On the other hand, in 5xTAE-Mg buffer, DNA nanostructures were assembled into nanobelts, similar to those observed in 10xTAE-Mg. However, the extent of protein-DNA coverage was notably reduced, suggesting that buffer concentration affects both the assembly pathway and the efficiency of protein attachment (Figure S16, Supporting Information).

After synthesis in high-concentration buffer and subsequent dialysis into 1xTAE-Mg buffer, all DNA nanostructures and SSRD-DNA nanostructures retained their original morphology. No disassembly was observed, indicating that the assembly pro-

cess is irreversible (Figure S17, Supporting Information). These findings support the hypothesis that both buffer conditions and protein-DNA hybridization jointly influence the morphological transformation of the DNA nanostructures.

2.3. Protein Functionalization of Nanofibers and Nanorods

2.3.1. Bifluorescent Functionalization of DNA Fibers

To further test the multilayer assembly of protein-DNA structures, DCV-GFP-SpyTag (DGSt) was designed for attaching SSRD. After mixing DGSt with SSRD-nanofiber or nanorod, the fluorescence of GFP and RFP was simultaneously detected by TIRF. Both nanostructures exhibited strong green fluorescence under 488 nm laser excitation and red fluorescence under 561 nm laser excitation, confirming the successful attachment of GFP on their surfaces (**Figure 4A,B**). In contrast, SSRD nanofibers and nanorods individually showed only weak red fluorescence under

**ADVANCED
SCIENCE NEWS**

www.advancedsciencenews.com

**NANO · MICRO
small**

www.small-journal.com

the 488 nm laser. IRM further revealed the morphology of nanostructures under visible light. SAXS analysis showed the model of DGSt and SSRD-2xDGSt fitted to the experimental data ($\chi 2$ = 1.10 and 3.68, respectively), with a Dmax of 9.1 and 17.3 nm, respectively (Figure S19, Supporting Information). Multi-layer assembly could proceed in any sequential order: by first mixing SSRD with DNA nanostructure and then adding DGSt, or by first mixing DGSt with SSRD and then adding DNA nanostructure. Neither of them interfered with the morphology of nanofibers or nanorods, while there was less GFP background if DGSt and SSRD were mixed first, so we chose this order to do further experiments. To further validate the generality of a multilayer assembly, a tetrahedron coiled-coil origami structure incorporating one SpyCatcher and two GFP molecules (named TET_ScGG) was isolated for covalent binding with DRSt. Similar bifluorescent functionality was achieved by attaching ScGG to DRSt. (Figure S18D,E,F, Supporting Information).

Since the distance between the two standout overhangs in DNA nanostructure is close to the hydrodynamic diameter of proteins, SSRD had a much lower density on the nanorod's surface than DRSt. Figure S20 (Supporting Information) shows SDS PAGE of protein-DNA composites mixed with DNA nanostructure at a 1:1 molar ratio overnight and filtered through Durapore PVDF 0.1 µm centrifugal filter. Protein-DNA attached to the nanofiber or nanorod remained on the membrane, and only the unattached molecules were removed by ultrafiltration. The results proved that the immobilization efficiency of SSRD-DNA$_{P2}$ was ≈50%, which was similar to SSRD-2xDGSt-DNA$_{P2}$, demonstrating that the multi-layer assembly of DGSt didn't disturb the immobilization. On the other hand, almost all DRSt-DNA$_{P2}$ were successfully immobilized onto DNA nanostructures. However, after assembling with TET_ScGG, the immobilization efficiency was reduced by half. The above results indicated that the immobilization yield can be regulated by protein size and the interval of DNA overhang. In both buffers, mixing DNA nanostructure and SSRD without DNA conjugation could not induce the formation of fibers or rods but only caused slight nonfluorescent aggregations (Figure S21, Supporting Information). This proved that the complementary sequence between protein-DNA$_{P2}$ composite and DNA nanostructure overhangs is the key factor in the synthesis of nanostructures.

2.3.2. Enzyme Functionalization of Nanomaterials

Enzyme immobilization has gained significant attention in industrial, medical, and environmental applications for its enhanced stability, reusability, efficiency, cost-effectiveness, reduced contamination, and ability to enable continuous processing and multi-step reactions.[47] Here we chose NanoLuc, a highly stable and versatile luciferase[48] as a model to test the prospect of enzyme functionalization on the surface of protein-DNA nanomaterials. The catalytic activity can be evaluated via luminescence at 460 nm, generated by the catalyzed oxidation of the substrate. Since the shortest emission wavelength filter of TIRF is 525–562 nm, we fused NanoLuc with GSt (construct name: LucGSt), and used SSRD-2xLucGSt for nanoLuc functionalized nanofiber and nanorod self-assembly, so that the signal can be detected through GFP fluorescence generated by the BRET.[49,50] Fluo-

rescence spectrophotometer confirmed the bioluminescence of NanoLuc-SpyTag (LucSt) at 460 nm, as well as the BRET signal of nanoLuc-GFP-SpyTag (LucGSt) at 520 nm (Figure S22, Supporting Information). To test the activity of the immobilized enzyme, nanoLuc-GFP functionalized nanofibers or nanorods were loaded into ibidi chambers and after the flow of the Nano-Glo luciferase assay mixture into the chamber, the BRET signal was detected without turning on any laser. The same sample was imaged using IRM or excited with 488 nm and 561 nm lasers simultaneously (Figure 4C,D). Overlays of green and red fluorescence confirmed the immobilization of both SSRD and LucGSt. Realtime TIRF also captured the catalytic process and the generation of the BRET signal (Video 5). Similar functionalization and catalytic activities were also obtained through the self-assembly of DGSt and NanoLuc-SpyCatcher (LucSc) (Figure S23, Supporting Information). Different protein structures were characterized by SAXS (Figures S24 and S25, Supporting Information). The results demonstrate that the self-assembly platform allows for the simultaneous co-assembly of fluorescent proteins and enzymes without inhibiting their function.

2.3.3. Protein-DNA Circuits for Reversible Regulation of Enzymatic Activity

Furthermore, we utilized protein-DNA hybrids based on DNA hybridization and strand displacement reaction to construct a sensitive circuit, which enables in situ, reversible, and controllable regulation of split luciferase's activity on the surface of composite nanostructures. Luciferase can be divided into two non-functional fragments (large domain: Luc_Lg and small domain: Luc_Sm) and reassembled into a functional enzyme when brought into proximity by interacting proteins or molecular partners.[51] First, we fused split luciferase with the DCV domain separately, along with the Spider Silk domain (Spid) to increase the solubility and production yield (St-Luc_Lg-DCV and Spid-Luc_Sm-DCV). After DNA conjugation, the two components (St-Luc_Lg-DCV-DNA$_{H5'}$ and Spid-Luc_Sm-DCV-$_{H3'}$) become adjacent to each other by hybridizing with two termini of a 72 bp flexible ssDNA (DNA$_H$) (**Figure 5A**). As shown in Figure 5C, the two split_luciferase-DNA components don't interact in the solution, since DNA $_{H5'}$ and DNA$_{H3'}$ are non-complementary. After adding DNA$_H$, a Spid-SplitLuc-circuit was formed and a strong luminescence signal was detected. When Spid domain in Spid-Luc_Sm-DCV was replaced with GFP, a BRET signal was detected as the two split components are brought into proximity through DNA hybridization (Figure 5D). Stopped-flow measurements revealed the self-assembly rate of two split luciferase circuits (Figure 5B). Interestingly, the half-life of the circuit was strongly affected by protein domains fused adjacent to split luciferase: GFP-SplitLuc-circuit self-assembly was much slower (t½ 25.2 s) compared to Spid-SplitLuc-circuit (t½ 85.5 ms). When another Spid domain was fused to Luc_Lg-DCV as well, 2xSpid-SplitLuc-circuit had comparable activity but an even longer t½ (39.4 s) (Figure S26, Supporting Information). Even though the assembly was less stable and the kinetics curve couldn't reach the plateau (probably due to the dissociation of two split components), SEC-MALS results confirmed the successful assembly of the circuit (Figure S27, Supporting Information). The
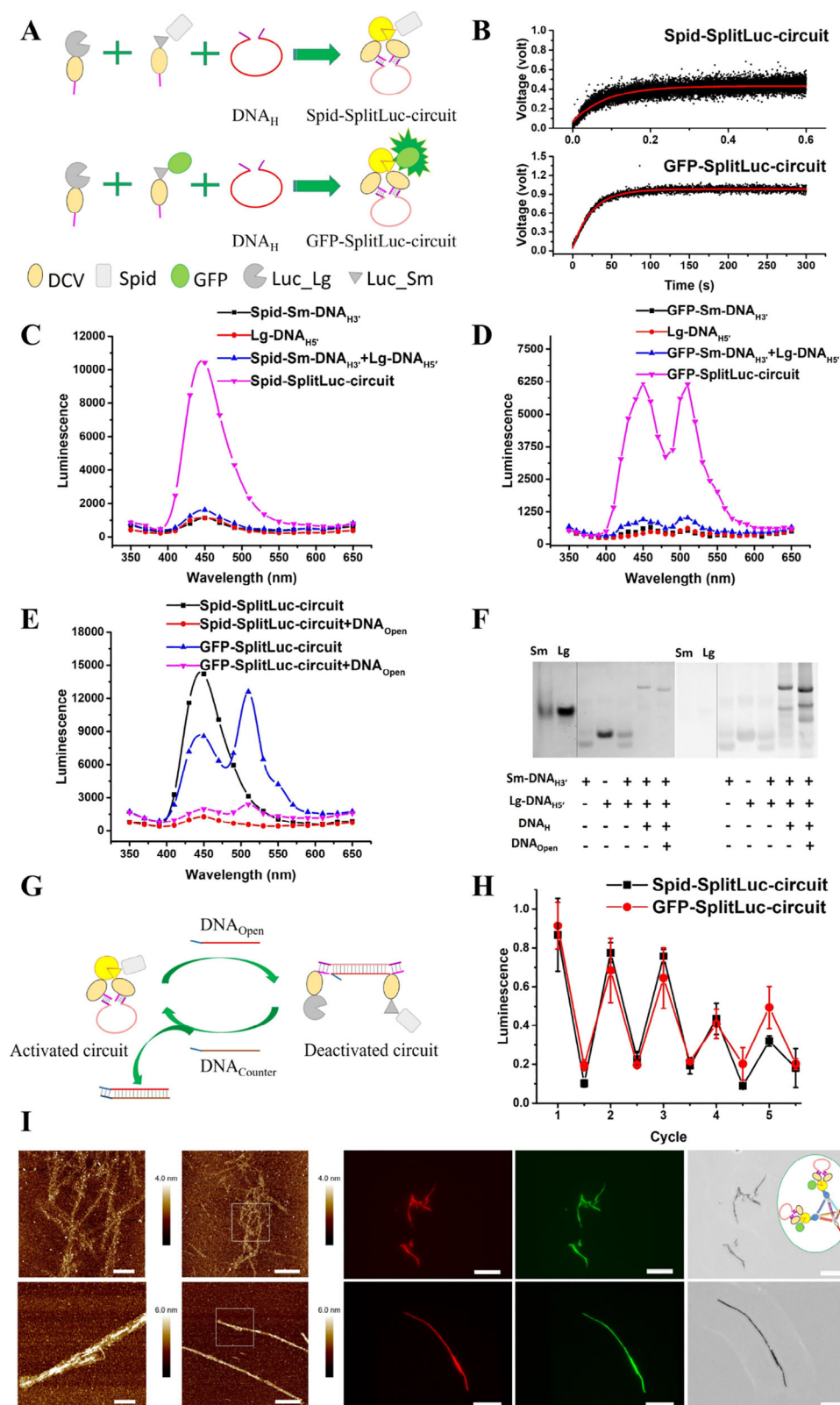
Figure 5. The synthesis and immobilization of protein-DNA circuits for reversible catalytic activity regulation. A) Self-assembling and enzyme activation mechanism of Spid-SplitLuc-circuit and GFP-SplitLuc-circuit. B) Stopped-flow measurements of Spid-SplitLuc-circuit (assembly rate: 11.69 s^{-1}, t$_{1/2}$: 85.5 ms) and GFP-SplitLuc-circuit (assembly rate: 0.040 s^{-1}, t$_{1/2}$: 25.2 s). One component fits are shown with red curves. C) Luminescence spectrum of Nano-Glo luciferase assay mixture in the presence of Spid-SplitLuc-circuit. Mixing two split NanoLuc composites doesn't lead to any catalytic activity,

ADVANCED
SCIENCE NEWS

www.advancedsciencenews.com

NANO · MICRO

small

www.small-journal.com

circuits were disrupted and opened in the presence of complementary DNA (DNA$_{Open}$), leading to the separation and inactivation of split luciferase (Figure 5E). Native PAGE stained with protein and DNA dye further confirmed the self-assembly and DNA hybridization (Figure 5F). As shown in Figure 5G, DNA$_{Counter}$ was used to release the circuits by removing DNA$_{Open}$ from DNA$_H$ through strand displacement reaction. Using this method, we achieved the on-off-on switching of functional loops and controllable regulation of enzyme activity. The bioluminescence variation demonstrated that both Spid-SplitLuc-circuit and GFP-SplitLuc-circuit could be repeatedly activated and deactivated (Figure 5H). After five cycles, the enzymes retained ≈50% activity.

To assess the structural stability of the protein-DNA switch, SDS-PAGE and native PAGE analysis of the Spid-SplitLuc-circuit before and after five cycles of DNA strand displacement regulation was performed (Figure S28, Supporting Information). During each cycle, DNA$_{Open}$ and DNA$_{Counter}$ were alternately added at increasing concentrations (1:1.1 ratio per addition). After five cycles, ≈90% of the circuit remained in the active state following DNA$_{Counter}$ addition, while nearly all circuits shifted to the inactive state after DNA$_{Open}$ addition. These results indicated that the strand displacement reactions were efficient and reversible. Moreover, no visible degradation or aggregation was observed in PAGE analyses, confirming the structural stability of the circuit. However, we noted a 35% decrease in the overall concentration of the Spid-SplitLuc-circuit after five cycles. This loss is likely due to cumulative dilution and nonspecific adsorption during repeated handling. Additionally, the gradual decline in enzymatic activity may be attributed to incomplete reassembly of the split luciferase caused by steric hindrance, misfolding, or suboptimal spatial orientation after multiple on-off transitions.

Furthermore, SpyTag fused at one of the split luciferase components was used to assemble the circuits with SSRD and DNA nanostructure (Figure 5I). As split luciferase's activity is much weaker than nanoLuc, the BRET signal can't be detected directly from TIRF. However, after immobilizing the GFP-SplitLuc-circuit onto nanofiber or nanorod, the fluorescence of both GFP and RFP was detectable and evenly distributed on the surface of nanostructures, indicating the successful self-assembly in both buffer conditions. To study the impact of immobilization on enzyme activity, DNA-protein composites, and non-conjugated proteins were mixed with DNA nanostructure at the same concentration (Figures S29 and S30, Supporting Information). To compare the effect of the tetrahedral protein on enzymatic catalytic activity, we designed a tetrahedral structure containing a single DCV and a single SpyCatcher (SD). Bioluminescence of catalytic reactions demonstrated that circuits had similar or even increased enzyme activity after the attachment to nanofibers or nanorods. The activity and BRET signal increased ≈2-fold only with DCV-GFP-SpyCatcher-DNA$_{P2}$ (DGSc-DNA$_{P2}$) and 2xSpid-SplitLuc-circuit. We hypothesized that SpyCatcher-SpyTag and two Spider Silk domains in between disturbed the proximity of split luciferase and strongly inhibited the BRET, while protein immobilization led to an increase in local density, thereby shortening the distance between two split components and GFP, consequently enhancing enzyme activity as well as BRET efficiency. Compared to a single SpyCatcher tetrahedral protein, SSRD bound two luciferase circuits at the same site, resulting in highly efficient functionalization with increased local enzyme density. Figure S31 (Supporting Information) showed that after immobilization, the enzyme activity of all the circuits could be regulated by a strand displacement reaction. The results indicate that our DNA-protein composite platform can readily self-assemble functional groups such as fluorescent proteins and enzymes on the surface of nanofiber or nanorods, and achieve controllable regulation of enzyme activity. This provides new possibilities for enzyme immobilization and the study of biocatalytic cascades.

3. Discussion and Conclusion

In this study, we report a modular platform that combines DNA-protein and protein-protein conjugation to build versatile and functional protein-DNA composites. DCV endonuclease domain was used for site-specific, covalent protein-DNA conjugation to circumvent limitations of traditional protein-DNA linkage strategies, such as the requirement for chemically modified DNA or the inefficiencies associated with non-covalent interactions. In parallel, the application of the SpyCatcher/SpyTag system allowed for modular protein-protein coupling, expanding the diversity and multivalency of the final assemblies. These orthogonal strategies proved to be highly compatible, enabling the construction of higher-order assemblies with tunable valency and spatial organization. The protein-DNA composites effectively directed the morphological transformation of DNA nanostructures, converting flexible nanotubes into either curvilinear nanofibers or rigid nanorods, depending on buffer conditions. This transformation suggests a cooperative assembly mechanism, where multivalent protein hubs nucleate and stabilize distinct DNA geometries.

Functionality was further demonstrated through the integration of fluorescent proteins and luciferase-based enzymes. We showed that bifluorescent labeling and enzymatic activity could be retained following immobilization on nanofibers and nanorods. The successful reconstitution and reversible control of split NanoLuc luciferase activity through strand displacement

---

and the luminescence signal shows up after DNA$_H$ connects the two components. D) Luminescence spectrum of Nano-Glo luciferase assay mixture in the presence of GFP-SplitLuc-circuit. Luminescence and BRET signals only show up after adding DNA$_H$ into the mixture. E) The catalytic activity of Spid-SplitLuc-circuit and GFP-SplitLuc-circuit regulated by DNA$_{Open}$ through strand displacement reaction. F) 10% Native gel of different Spid-SplitLuc-circuit components. Left: protein stained with Coomassie blue; Right: DNA stained with GelRed. G) Reversible activity regulation of split nanoLuc through DNA strand displacement reaction. H) Catalytic activity variation of Spid-SplitLuc-circuit and GFP-SplitLuc-circuit in five cycles of DNA strand displacement regulation. The error bars indicate the standard deviations of three measurements of independent samples for each cycle. I) Morphology characterization of GFP-SplitLuc-circuit functionalized nanofiber in 1xTAE-Mg buffer (up line) and nanorod in 10xTAE-Mg buffer (bottom line). From left to right: AFM image at the scale of 3 × 3 μm, scale bar: 0.5 μm; AFM image at the scale of 10 × 10 μm, scale bar: 2 μm, the 3 × 3 μm image scanning range was marked with a white square; TIRF image excited by 561 nm laser; TIRF image excited by 488 nm laser; IRM image. Scale bars of TIRF and IRM are 10 μm. The schematic shows the structure of SSRD-2xGFP-SplitLuc-circuit-DNA$_{P2}$.

**ADVANCED
SCIENCE NEWS**

www.advancedsciencenews.com

NANO · MICRO

small

www.small-journal.com

reactions highlights the potential of these assemblies as responsive, signal-generating devices. Importantly, this dynamic control did not compromise the structural integrity or enzymatic function of the system, establishing the feasibility of programmable biocatalysts on nanostructured surfaces.

A major strength of this approach lies in its ability to combine the spatial precision and programmability of DNA nanotechnology with the functional versatility of engineered proteins. Using components like SSRD and DRSt/DGSt, we show that proteins can be precisely positioned on DNA scaffolds to build layered, multifunctional nanostructures. Although it hasn't been tested in this paper, the orthogonal conjugation could also be controlled by other DNA binding domains such as MobA[41], or SilkCatcher-SilkTag[52], a compatible non-cross-reactive protein pair against SpyCatcher-SpyTag. All these protein-DNA blocks offer a set of orthogonal tools to expand the diversity of self-assembly and functionalization.

Compared to flexible linkers, the design of SSRD—with two defined conjugation sites—enables more precise placement of enzymes, improving their orientation and potential activity on nano-surfaces. By incorporating fluorescent proteins and enzyme circuits, we demonstrated reversible regulation of enzymatic function through DNA strand displacement, highlighting the dynamic potential of our system.

Overall, the presented platform creates a bridge between molecular design and functional nanomaterials. It supports the construction of smart, responsive bio-nanodevices with applications in synthetic biology, biomedicine, and materials science. The combination of programmability, modularity, and functionality makes this system a promising foundation for next-generation technologies in diagnostics, drug delivery, and dynamic biosensors.

4. Experimental Section

Materials: Chemicals in analytical reagents were purchased from Sigma–Aldrich. ssDNAs were purchased from Eurofins Genomics (Germany). Protein and DNA sequences are shown in Table S1 (Supporting Information) and Table S2 (Supporting Information).

Molecular Cloning: E. coli strain DH5-α (F− φ80lacZΔM15 Δ(lacZYA-argF) U169 recA1 endA1 hsdR17(rK−, mK+) phoA supE44 λ− thi-1 gyrA96 relA1) (NEB, MA USA) was used for plasmid propagation. The transformation was performed via heat shock at 42 °C for 2 min with competent E. coli cells. Single colonies were propagated in Lysogeny broth (LB) media with 50 µg ml⁻¹ antibiotic kanamycin (Goldbio, MO USA).

All the proteins were cloned in the expression vector pET41a(+) (Merck, Germany). The DNA sequences coding for the protein constructs were optimized for E. coli codon usage and subsequently purchased from Integrated DNA Technologies (IDT, USA). DNA sequences were inserted in the expression vector either via Golden Gate or Gibson assembly according to manufacturer instructions. BsaI-HFv2 restriction enzyme, T4 ligase, and T4 ligase buffer (NEB, MA USA) were used for Golden Gate assembly. Gibson assembly was performed with the enzymes Taq Ligase, Phusion Polymerase, and T5 exonuclease (NEB, MA USA). DNA purification was performed with Spin Miniprep Kit (QIAGEN, Germany).

Protein Production: E. coli strain NiCO21(DE3)44 was used for producing all the proteins (can::CBD fhuA2 [lon] ompT gal (λ DE3) [dcm] arnA::CBD slyD::CBD glmS6Ala ΔhsdS λ DE3 = λ sBamHIo ΔEcoRI-B int::(lacI::PlacUV5::T7 gene1) i21 Δnin5) (NEB, MA USA). Bacteria were grown at 37 °C in 100 mL LB media supplemented with 50 µg ml⁻¹ of kanamycin at 160 RPM agitation overnight. The pre-cultures were added into 1 L of LB media supplemented with 50 µg ml⁻¹ of kanamycin with a final concentration of 0.1 OD and left growing at 37 °C until OD values reached 0.6 to 0.9. Then the cultures were induced with 0.5 mm IPTG (Goldbio, MO USA) and grown at 30 °C, 160 RPM agitation for 4 h.

After production, the cultures were centrifuged at 5000 RPM (4 °C) to remove the media, then resuspended in lysis buffer (50 mm Tris-HCl pH 8.0, 150 mm NaCl, 10 mm imidazole, 0.06 µl ml⁻¹ Benzonase (Merck, Germany), 1 mm MgCl2, 2 µl ml⁻¹ CPI (Protease Inhibitor Cocktails, Millex Sigma–Aldrich, MO USA)). Cell lysis was completed by ultrasonication with a Vibra-cell VCX (Sonics, CT USA) on ice for 0.5 h at intervals of 2s pulse and 4 s pause (60% amplitude).

The cellular lysates were centrifuged at 16,000 g for 45 min (4 °C). The soluble fraction was filtered through 0.45 µm filter units (Sartorius stedim, Germany), and then flown through 5 ml Ni-NTA resin (Goldbio, MO USA) previously equilibrated with buffer A (50 mm Tris-HCl pH 8.0, 150 mm NaCl, 10 mm imidazole). After being washed with 500 mL buffer A and 500 mL buffer B (50 mm Tris-HCl pH 8.0, 150 mm NaCl, 20 mm imidazole), proteins were eluted with buffer C (50 mm Tris-HCl pH 8.0, 150 mm NaCl, 500 mm imidazole).

Strep-tag affinity was performed according to manufacturer instructions with 4 StrepTrap™ HP 5 ml columns (Cytiva, MA USA) connected in series and conditioned with SEC buffer (20 mm Tris-HCl pH 7.5, 150 mm NaCl). After binding and washing, the proteins were eluted with 2.5 mm d-Desthiobiotin (Millex Sigma-Aldrich, MO USA) dissolved in SEC buffer.

For size exclusion chromatography (SEC) we used HiLoad Superdex™ 200 resin (Cytiva, MA USA), packed in a 26/600 XK column (Cytiva, MA USA) equilibrated with filtered and degassed 10% glycerol SEC buffer (20 mm Tris-HCl pH 7.5, 150 mm NaCl, 10% glycerol v/v). Samples were injected into the column after filtration in 0.22 µm syringe filters (Millex Sigma–Aldrich, MO USA). AKTA pure fast protein liquid chromatography (FPLC) system (Cytiva, MA USA) was used to run the chromatography in SEC buffer with a linear flow rate of 2.6 ml min⁻¹.

After FPLC, proteins were frozen in liquid nitrogen and stored at -80 °C. Protein concentrations were determined by measuring absorbance at 280 nm utilizing the extinction coefficients calculated with ProtParam.

Protein-DNA Conjugation: To conjugate ssDNA to the DCV domain, protein, and DNA were mixed at a molar ratio of 1:1.1 in HEPES buffer (50 mm HEPES pH 8.0, 50 mm NaCl, 1 mm MgCl₂, 1 mm MnCl₂), then reacting at 37 °C, 300 rpm vibration for 2 h. Protein-DNA composite was separated from free DNA by Superdex™ 200 Increase 10/300 column (Cytiva, MA USA) in SEC-Mg buffer (20 mm Tris pH 7.5, 150 mm NaCl, 1 mm MgCl₂). The concentrations were calculated by DNA extinction coefficients at 260 nm.

Gel Electrophoresis: Samples were analyzed by native and SDS PAGE in a Bio-rad (CA USA) mini-PROTEAN™ apparatus in 10% discontinuous polyacrylamide gels at a voltage of 100 and 200 V, separately. Afterward, the gels were dyed with GelRed Nucleic Acid Gel Stain (Biotium, America) for DNA stain or InstantBlue™ (Millex Sigma–Aldrich, MO USA) for protein stain. Band densities were analyzed by Image Lab Software.

Size Exclusion Chromatography Coupled to Light Scattering (SEC-MALS): SEC-MALS analysis was conducted with an HPLC system (Waters, MA USA), coupled to a UV detector, a Dawn8+ multiple-angle light scattering detector (Wyatt, CA. USA), and a refractive index detector RI500 (Shodex, Japan). Protein-DNA samples were filtered through 0.1 µm centrifuge filters (Millex Sigma–Aldrich, MO USA) and applied to a Superdex™ 200 Increase 10/300 column in SEC-Mg buffer. Samples were injected at a concentration of ≈0.5 µm. Analysis of the peaks of interest was conducted with Astra 7.0 software (Wyatt, CA USA).

Small Angle X-ray Scattering (SAXS): Scattering curves of sample 22CC-1/2/3/4DCV were acquired with a table-top instrument SAXSpoint 5.0 (Anton Paar, AT) with primux 100 micro Cu X-ray generator and 2D 1 M EIGER2 R series detector at the National Institute of Chemistry (NIC), Slovenia. We used a heated/cooled sample cell holder, low-volume ASX autosampler, and the detector positioned at 600 mm from the measuring capillary. Samples 22CC-1/2/3/4DCV had a concentration of 8.6, 9.4, 7.9, and 8.2 mg/ml, respectively. A dilution series consisting of four different concentrations was performed for each of the samples to assess

**ADVANCED
SCIENCE NEWS**

www.advancedsciencenews.com

**NANO · MICRO
small**

www.small-journal.com

concentration effects. Each sample (20 µl) and their matching buffer was loaded into the 1 mm flow-through quartz capillary and the data were collected over 7 exposures each of 30 min. The temperature of the sample during measurements was kept at 10 °C via a Peltier unit. We used software SAXS Analysis by Anton Paar, (version 4.01) to transform and export the raw data. We used the ATSAS suite[58] to manually average the frames and to subtract the background of the buffer scattering.

SAXS results of other samples were measured at the P12 beamline that is part of the PETRA-III synchrotron at an X-ray wavelength of 1.24 Å (DESY, Hamburg, Germany). Scattering intensity was performed in the range from 0.028 to 6.6 nm^{-1} with the Pilatus 6 M detector, placed 3 m from the sample. All the protein samples were analyzed with SEC-SAXS. 3% glycol SEC buffer was used as a mobile phase to flow through the column (Superdex™ 200 increase 10/300) at a flow of 0.5 ml min^{-1}. 3600 scattering frames were collected with an exposure time of 0.995 s. ATSAS software was used for merging and data analysis. PepsiSAXS53 was used to compare experimental scattering profiles to model structures generated with the Robetta software. 10 000 random chain configurations were generated and the genetic algorithm was run 50 times to obtain a good ensemble fit.

DNA Tube and Protein-DNA Nanostructure Synthesis: DNA oligonucleotides were resuspended in Milli Q water, and quantitated by UV absorbance at 260 nm. Nanotubes were annealed at 1 µM final concentration in either TAE-Mg buffer (40 mM Tris, 20 mM acetate, 1 mM EDTA, 12.5 mm MgCl$_2$, pH 8.3) or 10x TAE-Mg buffer from 90 to 10 °C at 0.1 °C min^{-1}, and mixed with protein-DNA composites at 1:1 molar ratio, incubated at 4 °C overnight.

AFM Measurement: AFM images were obtained with a Nanoscope IIIa Multimode scanning probe microscope (Digital Instruments, Santa Barbara, USA) operating in tapping mode. A 10-micron range scanner was used to image protein-DNA oligomers and a 100-micron range scanner was used for nanorods and nanofibers. Samples were diluted to ≈0.01 µM, and spread across freshly cleaved mica surface. After incubating for 3 min at room temperature, samples were gently washed with Milli Q water and dried with a stream of nitrogen. Images were obtained by using standard tapping mode probes OTESPA (Mikromasch) with a tip radius below 7 nm and a nominal resonant frequency of 300 kHz at the scan rate of 1 Hz. The image resolution was 512 × 512 pixels. Raw images were processed with NanoScope Analysis software (Bruker, MA, USA).

DLS Measurement: The composition and size distribution of protein-DNA composites were measured on a Malvern Zetasizer (Malvern, UK) at 20 °C using an angle of 173° and 633-nm laser. 70 µL 0.3-0.5 µM sample was added into the cuvette and stabilized for 2 min before measurement.

Bioluminescence Measurement: The nano-Glo Luciferase Assay System was used to detect luciferase activity. The reacting reagent was made by mixing one volume of Nano-Glo Luciferase Assay Substrate with 50 volumes of Nano-Glo Luciferase Assay Buffer. Then protein-DNA samples (concentrations between 0.1 to 1 µM) were added to the reacting reagent at a 1:1 volume ratio. Bioluminescent spectra were measured by multi-plate fluorescence reader Synergy Mx (Bio TeK, VT USA) in 96-well plates.

Stopped-Flow Measurement: Kinetic analysis of SplitLuc-circuits was measured on a MOS-500 spectrometer with an SFM-3000 stopped-flow unit (BioLogic, France). The two protein-DNA components were loaded in Syringe 3 (volume capacity 1.9 mL), DNA$_H$ with Nano-Glo luciferase assay mixture was loaded in Syringe 2 (volume capacity 10 mL), and SEC-Mg buffer was loaded in Syringe 1 (volume capacity 10 mL). The total volume per measurement was 242 µL with a total flow rate of 2.5 mL s^{-1}. The final concentration of protein-DNA components and DNA$_H$ was 0.25 µM. The cuvette used was 1.5 by 0.5 mm in size (FC15/5). The instrument was set in fluorescent mode without turning on any laser. For Spid-SplitLuc-circuit and GFP-SplitLuc-circuit, the signal was recorded every 100 ms for 300 s, while for 2xSpid-SplitLuc-circuit, the signal was recorded each 0.05 ms for 0.6 s, each experiment was performed with four repetitions.

TIRF and IRM: 6 channel Ibidi 1.5H glass coverslip slides were cleaned using 2% Hellmanex (Sigma–Aldrich, MO, USA) solution and Milli Q water. Protein-DNA nanostructures were flushed into the chamber at a concentration of 0.05 to 0.5 µM. IRM and TIRF microscopy were performed on a LUMICKS C-TRAP EDGE 350 with a Nikon CFI Apo TIRF 60XC

Oil objective. For fluorescence measurement, images were excited with a 488 nm laser (for GFP) or 561 nm laser (for RFP) at 1% power (15.3 µMW). 525/40 and 600/50 emission filter was used accordingly. Integration time on the camera was 100 ms. The effective pixel size was 72 nm. For bioluminescence measurement, after samples were loaded into the chamber, the reacting reagents were flowed through via a Microfluidics system slowly. Then the videos were recorded with all the lasers off and without any flow. The integration time on the camera was 1000 ms. Images were viewed in Fiji 2.14/ImageJ 1.5.4f (https://www.nature.com/articles/nmeth.2019).

Supporting Information

Supporting Information is available from the Wiley Online Library or from the author.

Conflict of Interest

The authors declare no conflict of interest.

Author Contributions

The conceptualization was carried out by W. Z. The methodology was developed by W.Z. and M.Š. The investigation was conducted by W.Z., while visualization was performed by W.Z., J.S., and M.Š. Supervision was provided by R.J. The original draft was written by W.Z., J.S., M.Š., and R.J., and all authors contributed to the review and editing of the manuscript.

Data availability Statement

The data that support the findings of this study are available in the supplementary material of this article

[1] E. Benson, A. Mohammed, J. Gardell, S. Masich, E. Czeizler, P. Orponen, B. Högberg, *Nature* **2015**, *523*, 441.

[2] H. Jun, F. Zhang, T. Shepherd, S. Ratanalert, X. Qi, H. Yan, M. Bathe, *Sci. Adv.* **2019**, *5*, aav0655.

[3] S. M. Douglas, I. Bachelet, G. M. Church, *Science* **2012**, *335*, 831.

[4] Y. Ke, T. Meyer, W. M. Shih, G. Bellot, *Nat. Commun.* **2016**, *7*, 10935.

[5] P. Kosuri, B. D. Altheimer, M. Dai, P. Yin, X. Zhuang, *Nature* **2019**, *572*, 136.

[6] K. Nakazawa, F. El Fakih, V. Jallet, C. Rossi-Gendron, L. Mariconti, L. Chocron, M. Hishida, K. Saito, M. Morel, S. Rudiuk, D. Baigl, *Angew. Chem., Int. Ed.* **2021**, *60*, 15214

[7] C. Gatsogiannis, O. Hofnagel, J. Markl, S. Raunser, *Structure* **2015**, *23*, 93.

[8] G. L. Hura, J. A. Tainer, *Nat. Biotechnol.* **2017**, *35*, 1044.

[9] A. Ljubetič, H. Gradišar, R. Jerala, *Curr. Opin. Chem. Biol.* **2017**, *40*, 65.

[10] I. Drobnak, A. Ljubetič, H. Gradišar, T. Pisanski, R. Jerala, *Adv. Exp. Med. Biol.* **2016**, *940*, 7.

[11] A. Ljubetič, I. Drobnak, H. Gradišar, R. Jerala, *Chem. Commun.* **2016**, *52*, 5220.

[12] F. Lapenta, J. Aupič, M. Vezzoli, Ž. Strmšek, S. Da Vela, D. I. Svergun, J. M. Carazo, R. Melero, R. Jerala, *Nat. Commun.* **2021**, *12*, 939.

[13] T. Satler, S. Hadž, R. Jerala, *J. Am. Chem. Soc.* **2023**, *145*, 16995.

[14] J. Wang, S. Lisanza, D. Juergens, D. Tischer, J. L. Watson, I. Anishchenko, W. Yang, D. R. Hicks, M. Expòsit, T. Schlichthaerle, F. Dimaio, B. Correia, S. Ovchinnikov, D. Baker, *Science* **2022**, *394*, 387.

[15] K. Tapio, I. Bald, *Multifunct. Mater.* **2020**, *3*, 032001.

[16] Y. Sakai, M. Sirajul Islam, M. Adamiak, S. Chi-Chin Shiu, J. Alexander Tanner, J. Gardiner Heddle, *Genes* **2018**, *9*, 571

[17] P. Notin, N. Rollins, Y. Gal, C. Sander, D. Marks, *Nat. Biotechnol.* **2024**, *42*, 216.

[18] B. Saccà, R. Meyer, M. Erkelenz, K. Kiko, A. Arndt, H. Schroeder, K. S. Rabe, C. M. Niemeyer, *Angew. Chem.* **2010**, *122*, 9568.

[19] Q. Shen, Q. Xiong, K. Zhou, Q. Feng, L. Liu, T. Tian, C. Wu, Y. Xiong, T. J. Melia, C. P. Lusk, C. Lin, *J. Am. Chem. Soc.* **2023**, *145*, 1292.

[20] G. Kong, M. Xiong, L. Liu, L. Hu, H. M. Meng, G. Ke, X.-B. Zhang, W. Tan, *Chem. Soc. Rev.* **2021**, *50*, 1846.

[21] X. Xu, D. Han, C. Minireviews, *ChemPlusChem* **2021**, *86*, 284.

[22] N. Stephanopoulos, *Chem* **2020**, *6*, 364.

[23] C. Timm, C. M. Niemeyer, *Angew. Chem., Int. Ed.* **2015**, *54*, 6745.

[24] B. J. H. M. Rosier, A. J. Markvoort, B. Gumí Audenis, J. A. L. Roodhuizen, A. den Hamer, L. Brunsveld, T. F. A. de Greef, *Nat. Catal.* **2020**, *3*, 295.

[25] W. P. Klein, R. P. Thomsen, K. B. Turner, S. A. Walper, J. Vranish, J. Kjems, M. G. Ancona, I. L. Medintz, *ACS Nano* **2019**, *13*, 13677.

[26] J. Huang, A. Suma, M. Cui, G. Grundmeier, V. Carnevale, Y. Zhang, C. Kielar, A. Keller, *Small Struct.* **2020**, *1*, 2000033.

[27] J. Fu, M. Liu, Y. Liu, N. W. Woodbury, H. Yan, *J. Am. Chem. Soc.* **2012**, *134*, 5516.

[28] J. Jin, E. G. Baker, C. W. Wood, J. Bath, D. N. Woolfson, A. J. Turberfield, *ACS Nano* **2019**, *13*, 9927.

[29] A. Keppler, S. Gendreizig, T. Gronemeyer, H. Pick, H. Vogel, K. Johnsson, *Nat. Biotechnol.* **2002**, *21*, 86.

[30] G. V. Los, L. P. Encell, M. G. McDougall, D. D. Hartzell, N. Karassina, C. Zimprich, M. G. Wood, R. Learish, R. F. Ohana, M. Urh, D. Simpson, J. Mendez, K. Zimmerman, P. Otto, G. Vidugiris, J. Zhu, A. Darzins, D. H. Klaubert, R. F. Bulleit, K. V. Wood, *ACS Chem. Biol.* **2008**, *3*, 373.

[31] A. D. Keefe, D. S. Wilson, B. Seelig, J. W. Szostak, *Protein Expr. Purif.* **2001**, *23*, 440.

[32] K. Cervantes-Salguero, M. Freeley, R. E. A. Gwyther, D. D. Jones, J. L. Chávez, M. Palma, *Biophys. Rev.* **2022**, *3*, 031401.

[33] K. J. Koßmann, C. Ziegler, A. Angelin, R. Meyer, M. Skoupi, K. S. Rabe, C. M. Niemeyer, *ChemBioChem* **2016**, *17*, 1102.

[34] T. A. Ngo, H. Dinh, T. M. Nguyen, F. F. Liew, E. Nakata, T. Morii, *Chem. Commun.* **2019**, *55*, 12428.

[35] J. Hellmeier, R. Platzer, V. Mühlgrabner, M. C. Schneider, E. Kurz, G. J. Schütz, J. B. Huppa, E. Sevcsik, *ACS Nano* **2021**, *15*, 15057.

[36] A. Shaw, E. Benson, B. Högberg, *ACS Nano* **2015**, *9*, 4968.

[37] J. Huang, A. Jaekel, J. van den Boom, D. Podlesainski, M. Elnagar, A. Heuer-Jungemann, M. Kaiser, H. Meyer, B. Saccà, *Nature Nanotechnology* **2024**, *19*, 1521.

[38] Y. Dong, Y. Mao, *ChemBioChem* **2019**, *20*, 2422.

[39] M. Chandler, F. De La Cruz, F. Dyda, A. B. Hickman, G. Moncalian, B. Ton-Hoang, *Nat. Rev. Microbiol.* **2013**, *11*, 525.

[40] K. N. Lovendahl, A. N. Hayward, W. R. Gordon, *J. Am. Chem. Soc.* **2017**, *139*, 7030.

[41] K. N. Lovendahl, *Adaptation of HUH endonucleases for protein-DNA conjugation*, PhD Thesis, University of Minnesota, ProQuest LLC (2019), **2018**.

[42] J. Aupič, Ž. Strmšek, F. Lapenta, D. Pahovnik, T. Pisanski, I. Drobnak, A. Ljubetič, R. Jerala, *Nat. Commun.* **2021**, *12*, 940.

[43] X. Yang, J. Wei, Y. Wang, C. Yang, S. Zhao, C. Li, Y. Dong, K. Bai, Y. Li, H. Teng, D. Wang, N. Lyu, J. Li, X. Chang, X. Ning, Q. Ouyang, Y. Zhang, L. Qian, *ACS Synth. Biol.* **2018**, *7*, 2331.

[44] J. Röder, R. Fischer, U. Commandeur, *Small* **2017**, *13*, 1702151.

[45] L. N. Green, H. K. K. Subramanian, V. Mardanlou, J. Kim, R. F. Hariadi, E. Franco, *Nat. Chem.* **2019**, *11*, 510.

[46] P. R. O'Neill, K. Young, D. Schiffels, D. K. Fygenson, *Nano Lett.* **2012**, *12*, 5464.

[47] S. Lim, G. A. Jung, D. J. Glover, D. S. Clark, *Small* **2019**, *15*, 1805558.

[48] C. G. England, E. B. Ehlerding, W. Cai, *Bioconjugate Chem.* **2016**, *27*, 1175.

[49] H. Kobayashi, L. P. Picard, A. M. Schönegge, M. Bouvier, *Nat. Protoc.* **2019**, *14*, 1084.

[50] Y. Namkung, C. Le Gouill, V. Lukashova, H. Kobayashi, M. Hogue, E. Khoury, M. Song, M. Bouvier, S. A. Laporte, *Nat. Commun.* **2016**, *7*, 12178.

[51] T. Plaper, J. Aupič, P. Dekleva, F. Lapenta, M. M. Keber, R. Jerala, M. Benčina, *Sci. Rep.* **2021**, *11*, 9136.

[52] R. Fan, J. Hakanpää, K. Elfving, H. Taberman, M. B. Linder, A. S. Aranko, *Angew. Chem. Int. Ed.* **2023**, *62*, 202216371.

2502060 (12 of 12)